Production of ^{21}Ne in depth-profiled olivine from a 54 Ma basalt sequence, Eastern Highlands (37° S), Australia

Erin L. Matchan[a], Masahiko Honda[b], Timothy T. Barrows[c], David Phillips[a], Allan R. Chivas[d], L. Keith Fifield[e], Derek Fabel[b, 1]

[a]*School of Earth Sciences, The University of Melbourne, Parkville, VIC 3010, Australia..*

[b]*Research School of Earth Sciences, The Australian National University, Canberra, ACT 0200, Australia.*

[c]*Geography, College of Life and Environmental Sciences, University of Exeter, Exeter, Devon, EX4 4RJ, UK.*

[d]*GeoQuEST Research Centre, School of Earth and Environmental Sciences, University of Wollongong, NSW 2522, Australia.*

[e]*Department of Nuclear Physics, Research School of Physics and Engineering, The Australian National University, Canberra, ACT 0200 Australia*.

[1] Now at: Scottish Universities Environmental Research Centre, East Kilbride G75 0QF, UK.

Abstract

In this study we investigate the cosmogenic neon component in olivine samples from a vertical profile in order to quantify muogenic ^{21}Ne production in this mineral. Samples were collected from an 11 m thick Eocene basalt profile in the Eastern Highlands of southeastern Australia. An eruption age of 54.15±0.36 Ma (2σ) was determined from ^{40}Ar/^{39}Ar step-heating experiments (n=6) on three whole-rock samples. A ^{36}Cl profile on the section indicated an apparent steady state erosion rate of 4.7 ± 0.5 m Ma^{-1}. The eruption age was used to calculate *in situ* produced radiogenic ^{4}He and nucleogenic ^{3}He and ^{21}Ne concentrations in olivine. Olivine mineral separates (n=4), extracted from the upper two metres of the studied profile, reveal cosmogenic ^{21}Ne concentrations that attenuate exponentially with depth. However, olivine (Fo_{68}) extracted from below 2 m does not contain discernible ^{21}Ne aside from magmatic and nucleogenic components, with the exception of one sample that apparently contained equal proportions of nucleogenic and muogenic neon. Modelling results suggest a muogenic neon sea-level high-latitude production rate of 0.02 ± 0.04 to 0.9 ± 1.3 atom g^{-1} a^{-1} (1σ), or <2.5% of spallogenic cosmogenic ^{21}Ne production at Earth's surface. These data support a key implicit assumption in the literature that accumulation of muogenic ^{21}Ne in olivine in surface samples is likely to be negligible/minimal compared to spallogenic ^{21}Ne.

Keywords: cosmogenic ^{21}Ne; noble gases; olivine; muons; cosmogenic ^{36}Cl

1. Introduction

Bombardment of minerals in the Earth's crust by secondary cosmic radiation gives rise to a variety of nuclear reactions. The end products of these reactions are known as secondary *in situ* terrestrial cosmogenic nuclides, the study of which has many useful geological applications (Gosse and Phillips, 2001; Dunai, 2010). The reactions that produce cosmogenic nuclides are classified into three categories: spallation, muon interactions and neutron capture.

At depths exceeding about three metres, muon interactions become the major cosmogenic nuclide production mechanism (e.g. Lal, 1987; Brown et al., 1995). The dominant type of muon-induced reaction producing most cosmogenic nuclides down to ca. 100 hg cm^{-2} (equivalent to a depth of 30 m for rock density of 3 g cm^{-3}) is nuclear capture of negative slow muons, below which fast-muon induced reactions dominate (e.g. Heisinger et al. 2002a,b). In rock surfaces at sea level, the contribution

of muons to total cosmogenic nuclide production ranges from minor, (e.g. 1-4 % for ^{10}Be and ^{26}Al production in quartz; Brown et al., 1995; Heisinger and Nolte, 2000), to as much as 10% (e.g. ^{36}Cl production in calcite; Stone et al., 1998). Muogenic production of noble gas isotopes is relatively poorly understood because nuclear cross-sections have not been measured and there are fewer empirical measurements.

Constraining the muogenic component is imperative because the muon flux scales with altitude differently to the fast neutron flux (e.g. Lal 1988; Dunai, 2000), and muogenic production could be important for studies of longer exposure involving greater sample depths, and burial history (e.g. Balco and Shuster, 2009; Braucher et al., 2013).

In this paper we investigate the muogenic component of ^{21}Ne production in olivine. We analyse depth-profiled samples from an Eocene basalt flow exposed in a quarry in the Eastern Highlands of southeastern Australia. Whole-rock ^{36}Cl analyses were conducted on the same profile as an independent measure of the exposure history.

1.1. Cosmogenic neon production in olivine

In surface samples, it is generally assumed that the muogenic contribution to the cosmogenic neon budget is insignificant compared to the spallogenic component (e.g. Gillen et al., 2010; Schimmelpfennig et al., 2011). A major limitation for validating this assumption is that nuclear reaction cross-sections and probability factors have not been experimentally determined for muon-capture reactions on elements producing isotopes of neon. Therefore, these values currently have to be estimated from proxy reactions assumed to have similar energy profiles (e.g. Fernandez-Mosquera et al., 2010).

In olivine ($(Mg,Fe)_2SiO_4$), cosmogenic ^{21}Ne ($^{21}Ne_c$) is considered to be dominantly produced by the spallation reaction $^{24}Mg(n,\alpha)^{21}Ne$, with a minor component derived from reactions on Si (~20%) and trace amounts from reactions on Al, Na, Ca and Fe (e.g. Masarik and Reedy 1995; Leya et al., 1998; Masarik 2002). Although numerous studies have investigated cosmogenic ^{3}He ($^{3}He_c$) production in olivine (see review by Goehring et al., 2010), relatively few have considered $^{21}Ne_c$ production in this mineral. This is likely primarily due to the lower $^{21}Ne_c$ production rate in olivine of *ca.* 45 atom g^{-1} a^{-1} (dependent on Mg-content; Poreda and Cerling 1992) at sea-level high-latitude (SLHL), compared to 123 ± 4 atom g^{-1} a^{-1} SLHL for $^{3}He_c$ (1σ; Goehring

et al., 2010). It is also stressed that measurement of neon isotopes is more challenging than measurement of helium isotopes. In the case of $^{21}Ne_c$ analyses of Quaternary samples, olivine separates in the order of a gram are typically required given conventional mass spectrometer sensitivities (e.g. Amidon et al., 2009; Gillen et al., 2010; Espanon et al., 2014). Studies investigating $^{21}Ne_c$ production in pyroxene are less common, with $^{21}Ne_c$ SLHL production rates of approximately 20–50 atom g^{-1} a^{-1}, dependent on elemental composition and production rate calculation methods (e.g. Schaefer et al., 1999,2000; Niedermann et al. 2007).

1.2. Deconvolving the cosmogenic neon signature

As summarised by Graham (2002), the neon isotopic compositions of both Ocean Island Basalts (OIB) and Mid-Ocean Ridge Basalts (MORB) occupy a broad distribution, but $^{21}Ne/^{20}Ne$ values generally overlap with the atmospheric composition because atmospheric neon generally overwhelms mantle neon in these samples. Therefore, the trapped $^{21}Ne/^{20}Ne$ ratio in olivine can be assumed to be indistinguishable from the atmospheric composition in most cases ($(^{21}Ne/^{20}Ne)_{air}$ = 0.00296 ± 0.7% (Eberhardt et al., 1965)), avoiding the need for sample-intensive crushing experiments as routinely applied in characterising cosmogenic He in these samples.

In situ produced nucleogenic neon ($^{21}Ne_{nucleo}$) is an important consideration for rocks with crystallisation ages older than a few 100 ka. $^{21}Ne_{nucleo}$ is produced predominantly by the reaction $^{18}O(\alpha,n)^{21}Ne$ and to a lesser extent $^{24}Mg(n,\alpha)^{21}Ne$ (Wetherill, 1954). In both cases, α and n are produced as a result of local decay of U and Th. Nucleogenic production of ^{20}Ne and ^{22}Ne under normal mantle conditions is considered to be insignificant (Yatsevich and Honda, 1997). The production rate of $^{20}Ne_{nucleo}$ is extremely low (e.g. $^{20}Ne_{nucleo}$ ~2×10^{-21} cm^3STP g^{-1} a^{-1}, assuming a typical U concentration in olivine of 2 ppm; Yatsevich and Honda, 1997). This results in negligible amounts of $^{20}Ne_{nucleo}$ compared to a typical total ^{20}Ne content of >1×10^{-11} cm^3 STP g^{-1} in olivine (e.g. Gillen et al., 2010; Schimmelpfennig et al., 2011). Similarly, since the $^{21}Ne/^{20}Ne$ production ratio of cosmogenic Ne components in olivine is ~1 (Schafer et al., 1999), the contribution of cosmogenic ^{20}Ne can be ignored. Therefore, all ^{20}Ne in a sample may be regarded as magmatic, atmospheric or their mixture. Using the elemental composition of the sample and following the

approach of Ballentine and Burnard (2002), the more significant $^{21}Ne_{nucleo}$ contents may be calculated (see section 4.4).

2. Geological setting

2.1 Regional geology and geomorphology

Cenozoic basalt (*senso lato*) flows crop out along the eastern margin of Australia and range in age from *ca.* 70 Ma to <1 Ma. In New South Wales and Victoria many of these flows occur in an elevated terrain commonly referred to as the Eastern Highlands. Here, basalts mantle a deeply weathered early Paleozoic terrane. The relative timing of uplift of the Eastern Highlands and its relationship to Cenozoic volcanism remain contentious issues (see summary by Norvick, 2011). It is currently unresolved as to whether uplift of the Eastern Highlands was dominantly Mesozoic or Cenozoic. The available evidence suggests that the relative timing and magnitude of uplift varies across the Highlands (Norvick, 2011).

Apatite fission track studies indicate a distinct period of rapid denudation across south-eastern Australia during the Paleocene to mid-Eocene (*ca.* 60–45 Ma), corresponding to a Paleogene cooling event recorded in rocks from this region (Kohn et al., 2002). The Cenozoic climate of south-eastern Australia is thought to have transitioned from temperate in the Early Eocene to progressively more arid and cool (see review by Vasconcelos et al., 2008). Glaciation was confined to elevations ≥1800 m in the Pleistocene (Barrows et al., 2001). This included the Early Kosciuszko glaciation at ca. 59 ka (Barrows et al., 2001) and the Last Glacial Maximum, constrained at 17–20 ka by cosmogenic ^{10}Be exposure dating of moraines from the Snowy Mountains and Tasmanian highlands, with deglaciation occurring well before the Holocene (Barrows et al., 2002). Late Quaternary bedrock erosion in the south-eastern Highlands has been inferred to have been ≤ 5 m Ma^{-1} (Heimsath et al., 2001).

2.2 Local geology

The sampling site (Thompson's Pit quarry) is located at 36°52.35' S, 149°16.30' E, in the Monaro Volcanic Province (Wellman and McDougall, 1974b) of south-eastern New South Wales, approximately 5 km NE of the township of Bombala (Fig. 1). In the Monaro Volcanic Province, flows crop out over an area of ~4,000 km^2, with thicknesses of up to 400 m (Wellman and McDougall, 1974b), and are dominantly olivine tholeiites or basanites, with lesser alkali olivine basalts, hawaiites and

144 nepheline hawaiites (Kesson, 1973; O'Reilly and Zhang, 1995). The weathering
145 profile of underlying Paleozoic rocks commonly exceeds 10 m (Taylor et al., 1990).
146 The relatively flat erosional surface is covered by fluvial and lacustrine sediments up
147 to 70 m thick that either underlie or are locally intercalated with the basalt flows
148 (Wellman and McDougall, 1974b; Taylor et al., 1990). A total of 65 eruption centres
149 have been identified in the Monaro Volcanic Province, although the majority of these
150 have been so deeply eroded that only remnant volcanic plugs remain and
151 determination of flow provenance is not possible (Roach et al., 1994). Taylor et al.
152 (1990) proposed a regional pre-eruptive relief of 800 m for the southern Monaro
153 region, and a post-eruptive geomorphological history dominantly influenced by
154 erosion.

155 Whole-rock K-Ar ages reported for basaltic flows in the Nimmitabel-Bombala area
156 range from 53.2 ± 1.0 Ma to 34.0 ± 0.4 Ma (2σ; Taylor et al., 1990). In this area,
157 lacustrine sediments form a 150 m-thick sequence intercalated with basalt flows
158 (Taylor et al., 1990). A K-Ar age of 53.2 ± 1.0 Ma (2σ) was reported by Taylor et al.
159 (1990) for a sample collected from a site near Bombala.

3. Methods

3.1 Sampling

The rim of the quarry face sampled at Thompson's Pit has an elevation of 829 m. Topographic shielding of the locality is negligible. Although the surface appears erosional and is free from topsoil, at least 2–3 m of soil and weathered basalt overlie fresh basalt on another side of this quarry (Fig. 2), suggesting that a similar weathered layer may have existed at the sampling site before quarrying commenced.

Samples (n=16) were extracted from a single pit wall, spanning a vertical profile of 0–12.6 m. These samples are considered to represent a single flow on the basis of thin-section petrography and field observations. A distinctive texture is characteristic of all samples, with large plates of clinopyroxene (up to 3 mm across) ophitically intergrown with small plagioclase laths. Olivine is slightly more abundant than clinopyroxene, and olivine phenocrysts average 0.5 mm in grain size, ranging up to 1 mm across. Olivine rims are mostly altered to iddingsite. The groundmass contains dark alteration or mesostasis (~10% by volume) surrounding thin plagioclase laths.

Samples were chosen for analysis on the basis of their location within the vertical profile, and their unaltered appearance: three samples were chosen for $^{40}Ar/^{39}Ar$ whole-rock dating, spanning 1.6–11.1m depth (TP9, TP5 and TP15); eight samples were selected for extraction of olivine for neon and helium isotopic analysis, spanning 0.3-11.1 m depth (TP13, TP12, TP11, TP10, TP6, TP5, TP4, TP15); and four samples (TP16, TP12, TP11, TP10), spanning 0.0-1.6 m depth, were selected for ^{36}Cl analysis as an independent measure of the exposure history.

3.2 $^{40}Ar/^{39}Ar$ geochronology

Crushed samples (TP5, TP9 and TP15) were washed of dust, dried, and sieved to a 250-500 μm grain size. Whole-rock chips were handpicked from each sample using a binocular microscope, avoiding phenocrysts, altered fragments and large vesicles. Samples were cleaned in an ultrasonic bath with 5% HNO_3, followed by deionised water and acetone. Samples were loaded into aluminium foil packets in can UM#29, along with the flux monitor GA-1550 biotite (equivalent to MD2-biotite: 99.125 ± 0.038 Ma (Phillips et al., 2017)), and irradiated for 10 hours with Cd-shielding in position 5C of the McMaster Nuclear Reactor, Hamilton, Canada.

$^{40}Ar/^{39}Ar$ furnace step-heating analyses of six 30 mg whole-rock aliquots were conducted in the Noble Gas Laboratory in the School of Earth Sciences, University of Melbourne, using a VG3600 mass spectrometer equipped with Daly and Faraday detectors, generally following methods described previously by Matchan and Phillips (2011). Following overnight pre-baking at 600 °C, aliquots wrapped in tin foil were heated incrementally from an idle temperature of 300 °C up to a maximum of 1450 °C. Blank levels were monitored between analyses and found to be atmospheric, and insignificant (1–3 × 10^{-15} moles ^{40}Ar) compared to sample gas concentrations (typically ≥1 × 10^{-13} moles ^{40}Ar). Mass discrimination was determined prior to the first analysis by measuring multiple air aliquots from a Doerflinger pipette, yielding a weighted mean value of 1.0075 ± 0.2% (1σ) per atomic mass unit, assuming $(^{40}Ar/^{36}Ar)_{atm}$= 298.56 ± 0.31 (Lee et al., 2006).

Argon isotopic results (Supplementary Table S1) are corrected for system blanks, mass discrimination, radioactive decay since neutron irradiation (^{37}Ar and ^{39}Ar), reactor-induced interference reactions and atmospheric argon. Decay constants used are those reported by Steiger and Jäger (1977). Correction factors (±1σ) for interfering isotopes were $(^{36}Ar/^{37}Ar)_{Ca}$ = 0.000289 (± 1.7%), $(^{39}Ar/^{37}Ar)_{Ca}$ = 0.000680 (± 2.8%), $(^{40}Ar/^{39}Ar)_{K}$ = 0.000400 (± 100%), and $(^{38}Ar/^{39}Ar)_{K}$ = 0.0130 (± 38.5%). $^{40}Ar/^{39}Ar$ ages were calculated relative to a GA-1550 biotite age of 99.125 ± 0.038 Ma (Phillips et al., 2017). Age spectra were generated using ISOPLOT (Ludwig, 2012) and plateau ages are defined as including >50% of the total ^{39}Ar released, distributed over at least 3 contiguous steps, with $^{40}Ar^{*}/^{39}Ar$ ratios within agreement of the mean at the 95% confidence level (see McDougall and Harrison, 1999).

3.3 Olivine major- and trace-element geochemistry

The major-element concentrations of four olivine samples (TP10, TP12, TP13 and TP15) were determined by XRF analysis at the University of Wollongong (Table 2).

In order to estimate *in situ* radiogenic helium ($^{4}He^{*}$), nucleogenic helium ($^{3}He_{nucleo}$) and nucleogenic neon ($^{21}Ne_{nucleo}$) contents, trace element contents of olivine (n=7) and groundmass (n=7) separates extracted from samples used in the neon study were measured via ICP-MS. This was undertaken at the School of Earth Sciences, the University of Melbourne, using an Agilent 7700x mass spectrometer, following procedures modified from Eggins et al. (1997) and Kamber et al. (2003). U, Th and Li

contents are given in Table 5 (full dataset provided as Supplementary Table S2). Mean concentrations of U, Th and Li in the groundmass are 1.6(±1.0%), 6.6(±1.0%), and 7.2(±1.5%) ppm, respectively. Olivine aliquots TP5, 4, 15 exhibit U and Th concentrations of 0.2 - 0.3 ppm, two to three times greater than other aliquots, likely reflecting a lower contribution from more primitive mantle olivine xenocrysts in these samples.

3.4 Neon and helium measurement

Olivine was separated from the 100-150 μm crush fraction using a combination of heavy liquid (methylene iodide ~3.3 g ml^{-1}) and magnetic separation techniques. Step-heating analyses of ~1 g olivine separates (n=8) were undertaken in the Noble Gas Laboratory at the Australian National University using a VG5400 noble gas mass spectrometer connected to a tantalum double-vacuum resistance furnace, following procedures previously described by Gillen et al. (2010). Individual olivine separates were enclosed in tin foil packets and baked overnight at ~75°C to remove adsorbed air. Furnace blanks were measured and noble gas isotope ratios were determined to be atmospheric in composition. Samples were heated to 500°C for 30 minutes (ramp time 20 minutes), followed by fusion at 1900°C, with helium and neon isotopes measured in the gas released from each step. Helium measurements were calibrated against the HESJ Pipette (Matsuda, 2002) using procedures described by Espanon et al. (2014), and neon was calibrated against the Heavy Gas Standard pipette, prepared from air (see Honda et al., 1993).

Mass-interference corrections (interference on ^{20}Ne from $^{40}Ar^{2+}$, ^{21}Ne from CH_2CO^{2+}, and ^{22}Ne from $CO_2{}^{2+}$ on ^{22}Ne) were minor (<1%) compared to the neon abundances measured in these samples. Between analyses the furnace was outgassed at ~1750-1850°C for ≥30 minutes and high-T (1600°C) blank levels were measured. Procedural blank-levels were checked directly prior to each analysis and the furnace was degassed repeatedly until background levels were acceptably low. ^{4}He and ^{20}Ne blanks for all extraction temperatures were $2.2 - 7.0 \times 10^{-10}$ and $3.7 - 7.1 \times 10^{-12}$ ccSTP, respectively. Blank corrections were negligible for all samples. Following the procedure of Honda et al. (1993), a series of algorithms were used to monitor and propagate correlated errors in isotopic ratios to calculate stated analytical errors.

3.5 ^{36}Cl extraction and measurement

Chlorine was extracted from whole-rock samples using standard procedures (e.g. Stone et al., 1996). The isotopic ratio of $^{36}Cl/Cl$ was measured by accelerator mass spectrometry on the 14UD accelerator at the Australian National University. The abundances of major target elements were determined by XRF. The concentrations of trace elements with large neutron capture cross sections (B, Gd, and Sm) and neutron-producing elements (U and Th) were measured by ICP-MS. Chlorine content was determined by isotope dilution. Chemical data are summarised in Table 3 (full dataset: Supplementary Table S3).

4. Results

4.1 Eruption age

Step-heating experiments for all 6 aliquots yielded $^{40}Ar/^{39}Ar$ plateau ages (Table 1; Fig. S1). Spectra generally exhibit descending staircase spectra, with older apparent ages from the lower-temperature step data (≤1000°C) likely reflecting the release of extraneous argon from low-retention sites. Plateau ages, typically constructed from the mid- to high-T steps, range from 54.55 ± 0.27 ka (2σ; TP9a) to 55.59 ± 0.44 (2σ; TP15b). Inverse isochron analysis reveals that initial ('trapped') $^{40}Ar/^{36}Ar$ values ($^{40}Ar/^{36}Ar_i$, Table 1; Fig. S1) are consistently higher than the atmospheric ratio ($(^{40}Ar/^{36}Ar)_{air}$ = 298.56 ± 0.31 (Lee et al., 2006)), suggesting the presence of extraneous argon (e.g. Singer et al., 1998) in all samples. As a consequence, the plateau ages, which were calculated assuming an atmospheric $^{40}Ar/^{36}Ar$ ratio for the trapped component, may be significantly older than the eruption/cooling age. Thus inverse isochron ages, which are typically at least 0.5 Ma younger than corresponding plateau ages, are preferred.

All six aliquots yield statistically indistinguishable inverse isochron ages (Table 1). The $^{40}Ar/^{36}Ar_i$ values for the two aliquots of sample TP5 are distinct (502 ± 150 (2σ, TP5a); 316 ± 12 (2σ, TP5b)), suggesting a heterogeneous contribution of extraneous argon in this sample, likely from mantle-derived excess argon residing in inclusions contained within olivine and pyroxene phenocrysts, and/or from mantle xenocrysts. Therefore, it was not valid to pool data from these two aliquots to form a composite inverse isochron. Rather, the eruption age of TP5 was estimated by calculating a weighted mean age from the inverse isochron ages of the two aliquots: 54.55 ± 0.66 Ma (2σ). Given the poorly constrained trapped $^{40}Ar/^{36}Ar$ compositions for the

remaining aliquots, this approach was also applied to samples TP9 and TP15, yielding indistinguishable weighted mean ages of 54.00±0.61 Ma (2σ) and 53.96±0.62 Ma (2σ) for TP9 and TP15 respectively.

An overall weighted mean age of 54.15±0.36 Ma (2σ, MSWD = 1.1) was calculated from the three weighted mean isochron ages (Table 1) and is considered to best reflect the eruption age of the basalt. This value is in agreement with previously determined K-Ar ages for basalts in the Nimmitabel-Bombala area reported by Taylor et al. (1990).

4.2 Theoretical $^{21}Ne_c$ production rates in olivine

Forsterite contents of all samples are in the range 66–69% (Table 2). Therefore, regardless of trace element variations, theoretical sea-level high-latitude (SLHL) spallogenic production rates for ^{21}Ne and ^{3}He should be identical for all olivine samples. Based on average major element concentrations (Table 2), a theoretical SLHL production rate of $^{21}Ne_c$ in TP olivine (Fo_{68}) was calculated to be 37 ± 7 (1σ, atom g^{-1} a^{-1}) and this value is used in the present study. This assumes spallogenic production only and utilises elemental production rates estimated by Masarik (2002). A slightly higher value (but consistent within 2σ uncertainty) of 50 ± 6 (1σ, atom g^{-1} a^{-1}) is calculated when assuming a SLHL $^{3}He_c$ production rate of 123 ± 4 (1σ, atom g^{-1} a^{-1}) and employing the $^{21}Ne_c/^{3}He_c$ production ratio of 0.41 (± 12%, 1σ) for Fo_{49} (Poreda and Cerling, 1992). As for $^{36}Cl_c$, the SLHL spallation production rate for $^{21}Ne_c$ (37 atom g^{-1} a^{-1}) was scaled to the TP locality using a scaling factor of 1.81, yielding a value of 66 ± 13 (1σ) atom g^{-1} a^{-1}. Changes in geomagnetic field strength, latitude or elevation were not considered because variations in these parameters are expected to be small compared to the uncertainty associated with the exposure history of the site.

4.3 Helium and neon isotopic composition of olivine

Helium and neon data from step-heating experiments (n=8) are summarised in Table 4 (see also Table S4-A for complete dataset), and neon data are presented in three-isotope space (Fig. 3). Total gas $^{3}He/^{4}He$ ratios generally decrease with depth, ranging from ~200 × 10^{-9} (or 0.14 R/R_a, where R_a is atmospheric $^{3}He/^{4}He$ ratio of 1.4 × 10^{-6}) in samples from the top 1 m (TP13, TP12, TP11), to ~50 × 10^{-9} (or 0.036 R/R_a) in samples from > 4 m depth. Relatively high $^{3}He/^{4}He$ ratios observed in the shallow-

depth samples, compared to those in deep-seated samples, likely reflect the addition of cosmogenic He to these samples. However, as will be discussed in later sections, significant fractions of cosmogenic He appear to have been lost from the samples when compared with coexisting cosmogenic Ne abundances.

$^{21}Ne/^{20}Ne$ isotope ratios for the 500°C step are consistently within 2σ uncertainties of the atmospheric value ($^{21}Ne/^{20}Ne_{air}$ = 2.96 ± 0.02 ✖10^{-3} (1σ)), with the exception of TP5, TP11, and TP15, which yielded slightly higher $^{21}Ne/^{20}Ne$ ratios of 4.43 ± 0.26 ✖10^{-3} (1σ), 3.85 ± 0.35 ✖10^{-3} (1σ), and 3.73 ± 0.33 ✖10^{-3} (1σ), respectively. $^{21}Ne/^{20}Ne$ isotope ratios for total gas summations show a broad inverse correlation with sample depth, ranging from ~8 ✖ 10^{-3} in samples from the top 1 m, down to 5 ✖ 10^{-3} in the deepest samples. The high $^{21}Ne/^{20}Ne$ isotope ratios observed in shallow-depth samples are due to the addition of spallogenic Ne whereas $^{21}Ne/^{20}Ne$ ratios in deep-seated samples represent a mixture of atmospheric, in-situ produced nucleogenic and possibly muogenic Ne, discussed below. The exception to this trend is sample TP11 (1.1 m), which yields an anomalously high $^{21}Ne/^{20}Ne$ value of 31.14 ± 1.26 ✖ 10^{-3}. Sample TP10 (1.6 m) also yielded anomalous neon isotope data, including an elevated $^{22}Ne/^{20}Ne$ ratio compared to the atmospheric value. A hole was discovered in the tantalum crucible following the analysis of TP11; therefore data from TP11 and TP10 are considered compromised and are excluded from further discussion.

In the low-temperature gas fraction (500 ^{o}C), $^{22}Ne/^{20}Ne$ isotope ratios are lower than the atmospheric value of 0.102 (Eberhardt et al., 1965), and Ne data lie on the mixing line between MORB (Sarda et. al, 1988) and atmosphere. This observation suggests that a magmatic component in the olivine samples in the current study is MORB-like, and it is trapped in fluid inclusions of olivine phenocrysts, as commonly observed (e.g., Graham, 2002). The fraction of magmatic Ne in these samples will constrain magmatic He expected to be observed, using a mantle He/Ne elemental abundance ratio.

4.4 Calculation of $^{4}He^{*}$, $^{3}He_{nucleo}$ and $^{21}Ne_{nucleo}$ components in olivine

Concentrations of *in situ* produced nucleogenic and radiogenic components were estimated for olivine assuming an eruption age of 54.15 ± 0.36 Ma (2σ), with results reported in Table 5 (see also Supplementary Table S4-B). Radiogenic ^{4}He ($^{4}He^{*}$) abundances were estimated using the approach of Blard and Farley (2008), and the U

and Th concentrations determined by ICP-MS. The production rate of $^{3}He_{nucleo}$ in olivine was calculated using the method of Andrews (1985). Neutron capture probabilities specific to individual sample compositions (namely Li, Na, Mg, Al, Si, Ca, U and Th) were calculated using nuclear cross-section values reported by Andrews and Kay (1982). A mean grain diameter of 500 μm was assumed for olivine phenocrysts in the calculation of net $^{4}He^{*}$ production, incorporating α loss/implantation (Blard and Farley, 2008). Calculated net $^{4}He^{*}$ concentrations for olivine range from $50 – 110 \times 10^{12}$ atom g^{-1}, while $^{3}He_{nucleo}$ concentrations range from $0.6 – 1 \times 10^{6}$ atom g^{-1}. The calculated $^{4}He^{*}$ and $^{3}He_{nucleo}$ for individual samples are listed in Table 5. The ^{4}He concentrations observed in the samples are consistent with those predicted between 82% (TP4) and 150% (TP12), and thus significant $^{4}He^{*}$ loss was not observed.

Based on O and Mg contents for individual samples (Table 2) and the empirical $^{21}Ne_{nucleo}$ production rate formulated in Ballentine and Burnard (2002), $^{21}Ne_{nucleo}$ concentrations are calculated (Table 5). Where O and Mg contents were unavailable, average O (41.4 wt%) and Mg (16.5 wt%) contents of four measurements in the present study (Table 2) were used. Because O and Mg contents in the olivine samples are lower than those for average mantle, the calculated $^{21}Ne_{nucleo}/^{4}He^{*}$ production ratio of 4.1×10^{-8} is slightly lower than the mantle value of. 4.6×10^{-8} (± 5%; Yatsevich and Honda, 1997). Calculated values for $^{21}Ne_{nucleo}$ range from $2.0–4.7 \times 10^{6}$ atom g^{-1} (production rates of 0.03–0.09 atom g^{-1} a^{-1}), reflecting variation in olivine U and Th contents. Thus $^{21}Ne_{nucleo}$ is calculated at 3–4% of the total ^{21}Ne concentration ($^{21}Ne_{meas}$) present in the shallower samples (TP13, TP12), and approximately 40% of that in the deeper samples (TP6, TP5, TP4, TP15). Associated errors for calculated *in situ* component concentrations are estimated to be 10% (1σ).

4.5 $^{36}Cl_c$ erosion rate

To determine an integrated long-term steady-state erosion rate for the upper 160 cm of the profile (TP16, TP-10, TP11, TP12), a best fit to the data (Table 4) was determined using the production of ^{36}Cl with depth. We calculated total production from spallation on K, Ca, Ti and Fe, and muon capture on K and Ca, using published production rates by Stone et al. (1996a; 1996b; 1998), Evan, (2001), and Masarik (2002). We assumed muon contributions of 5% for Fe and Ti. For ^{36}Cl production by neutron capture on K and Cl we followed the procedures of Liu et al. (1994), Phillips

et al. (2001) and Stone et al. (1998). The nucleogenic contribution was determined following Fabryka-Martin (1988) and was subtracted from the total ^{36}Cl to determine cosmogenic $^{36}Cl_c$. Calculated $^{36}Cl_c$ concentrations attenuate exponentially with depth, ranging from $9.10 \pm 0.19 \times 10^5$ atoms g^{-1} for the surface sample, to $1.85 \pm 0.11 \times 10^5$ atoms g^{-1} for the 160 cm depth sample (Table 4). The production rates were scaled at the surface using the scheme of Stone (2000) using nucleon and muon scaling factors of 1.810 and 1.343. An attenuation length of 160 $g.cm^{-2}$ was used for spallation together with a measured average density of 2.96 $g.cm^{-3}$. Chemical composition of the profile for ^{36}Cl production was assumed to be an average of all four samples. Water content was assumed to be zero. The attenuation of muons with depth was estimated using the approach of Granger and Smith (2000). No corrections were applied for changes in geomagnetic field strength through the exposure history.

The erosion rate determined is 4.7 ± 0.5 m Ma^{-1}, assuming the erosion has reached steady state. One sample (TP10) was an outlier (5σ outside the best fit for other samples). However, given the depth of this sample and its low concentration, its exclusion does not have a measureable effect on the erosion rate calculation. This rate is lower than the apparent erosion rate calculated for the uppermost sample alone (TP16 at 5 cm depth) of 5.8 ± 0.6 m Ma^{-1}. The difference between the two measurements is resolved by adding a former cover of ~30 g cm^{-2} (~20 cm of soil at 1.5 g cm^{-3}) above TP-16. The $^{36}Cl_c$ data reflect conditions during the last ~0.5 Ma only given the ^{36}Cl half-life of 301 ka and the apparent erosion rate.

5. Discussion

5.1 Comparison of helium and neon contents in olivine

Once the $^4He^*$ and $^3He_{nucleo}$ components are accounted for, the decrease in the total $^3He/^4He$ ratio with increasing sample depth likely reflects a diminishing cosmogenic signal, although it is not possible to quantify ^3He_c for reasons discussed below.

$$^3He_c = {}^3He_T - \left[\left({}^4He_T - {}^4He^* \right) \times \left(\frac{^3He}{^4He} \right)_{mag} \right] - {}^3He_{nucleo} \quad (1)$$

$^{3}He_c$ is calculated as per Equation 1. In order to discuss quantitative loss of $^{3}He_c$ in the samples, in the following we will compare pairs of mantle He and Ne and cosmogenic He and Ne, and demonstrate that both mantle He and cosmogenic He are elementally depleted, relative to the corresponding Ne components.

As demonstrated in Figure 3, at the lower extraction temperature of 500 °C mantle Ne is released and data lie on the mixing line between atmospheric and MORB Ne (Sarda et al., 1988). Using $^{22}Ne/^{22}Ne$ ratios of the two Ne endmember components [$(^{22}Ne/^{20}Ne)_{solar}$ = 0.0727 (Benkert et al. 1993; Grimberg et al., 2006) and $(^{22}Ne/^{20}Ne)_{atmospheric}$ = 0.102 (Eberhardt, et al, 1965)], concentrations of mantle ^{20}Ne are calculated for samples TP5 and TP6 where the largest $^{22}Ne/^{20}Ne$ isotope anomalies relative to atmospheric have been observed in the current dataset (Table 4), and they are 2.1×10^{8} and 1.6×10^{8} atom g-^{1}. Using a $^{3}He/^{20}Ne$ ratio for the upper mantle of 0.75 (Honda and McDougall, 1998; Tucker and Mukhopadhyay, 2014), the corresponding mantle ^{3}He concentrations expected to be observed in the samples are 1.6×10^{8} and 1.6×10^{8} atoms g^{-1} for TP5 and TP6, respectively. In contrast, the total ^{3}He concentrations actually observed in the samples, which could be a mixture of cosmogenic, nucleogenic and mantle He are 6.4×10^{6} and 6.1×10^{6} atoms g^{-1}, respectively. Thus, it appears that mantle He was preferentially lost, relative to mantle Ne, from the TP samples.

A similar approach can also be applied when evaluating cosmogenic He and Ne in the TP samples. As will be demonstrated effectively 100% of excess ^{21}Ne, relative to atmospheric neon, in the shallow-depth samples TP13 and TP12 is spallogenic (Table 5). Using the cosmogenic $^{21}Ne_c/^{3}He_c$ production ratio of 0.41 for olivine (Poreda and Cerling, 1992), $^{3}He_c$ concentrations expected to be observed in samples TP13 and TP12 can be calculated as 2.7×10^{8} and 2.0×10^{8} atom g^{-1}, respectively, while the total ^{3}He concentrations observed in these samples are 1.9×10^{7} and 1.4×10^{7} atom g^{-1}, respectively. Similar to the case for mantle He, substantial amounts of cosmogenic He appear to have been lost from the TP samples. In contrast, $^{4}He^*$ produced in-situ appears to be retained in the olivine samples, which may reflect different trapping sites for $^{4}He^*$, $^{3}He_c$ and mantle He.

5.2 Cause of cosmogenic He loss

As has previously been proposed (e.g. Blard et al., 2008), some fluid inclusions may be broken during the sample crushing process, leading to some loss of magmatic

helium. However, magmatic ^{4}He has been demonstrated to have a lower diffusivity than matrix-sited ^{4}He (Blard et al, 2006; Tolstikhin, 2010); therefore some cosmogenic He may have also been lost during crushing, as cosmogenic He is matrix-sited. Furthermore, although olivine is highly retentive of helium at surface temperatures (e.g. Trull, 1991), it is possible that some helium, including cosmogenic He, may have been lost from secondary phases in weathered olivine. It has also been recently demonstrated (Protin et al, 2016), that underestimation of $^{3}He_c$ in olivine grains <200 μm may result from overestimation of magmatic ^{3}He due to contamination from atmospheric helium irreversibly adsorbed during crushing and storage under air.

5.3 *Neon in the samples*

In the case of neon, the isotopic composition of gas liberated from the initial (500°C) heating step suggests a trapped component comprising a mixture of atmospheric and mantle (MORB-like) neon (Fig. 3). The exceptions to this are samples TP11 and TP10, which (as noted in section 4.3) yielded anomalous data, probably reflecting damage to the furnace crucible. The $^{22}Ne/^{20}Ne$ and $^{21}Ne/^{20}Ne$ ratios measured in gas released during the fusion (1900 °C) step plot within error of the mixing line between spallogenic and atmospheric neon. However, in samples from depths exceeding three metres, negligible contribution from spallogenic $^{21}Ne_c$ is expected. Thus the elevated $^{21}Ne/^{20}Ne$ ratios observed in fusion of deep samples (TP6 TP5 TP4 and TP15) likely reflect ingrowth of nucleogenic neon, and the fact that isotopic ratios plot on the spallation line may be coincidental. Nucleogenic production of ^{22}Ne and ^{20}Ne is insignificant in olivine, compared to ^{21}Ne (Yatsevich and Honda, 1997; Ballentine and Burnard, 2002). Therefore, accumulation of nucleogenic neon will serve to translate data to the right in neon 3-isotope space (Fig. 3). The proportional increase of $^{21}Ne_{nucleo}$ with depth is readily explained by decreasing contributions from spallation reactions, although this effect is partially obscured by variations in U and Th concentrations (Table 5).

Excess ^{21}Ne (hereafter referred to as $^{21}Ne_{excess}$), relative to atmospheric Ne, is defined as all ^{21}Ne remaining after subtraction of the atmospheric component ($^{21}Ne_{air}$), as described by Equation 2:

$$^{21}Ne_{excess} = {}^{20}Ne_{meas} \times [(^{21}Ne/^{20}Ne)_{meas} - (^{21}Ne/^{20}Ne)_{air}] \quad (2)$$

('meas' denotes measured concentration).

Thus $^{21}Ne_{excess}$ comprises a mixture of mantle (i.e. solar), *in situ* produced nucleogenic and cosmogenic (spallogenic ± muogenic) components. The contribution of mantle neon to $^{21}Ne_{excess}$ can be assessed by considering the $^{22}Ne/^{20}Ne$ ratio of gas released in the initial heating step: the excess ^{21}Ne calculated for this lower temperature (500°C) fraction is assumed to be mantle-derived ^{21}Ne residing in fluid inclusions, (e.g. Graham, 2002) as supported by the distribution of data in neon three-isotope space along the air-MORB mixing line (Fig. 3). In the case of samples TP6 and TP5, the $(^{22}Ne/^{20}Ne)_{meas}$ ratio for the initial step is marginally lower than the air value at the 2σ uncertainty level, such that $^{21}Ne_{mantle}$ is significant in these samples. However, this is relatively minor (Table 6), with $^{21}Ne_{mantle}$ comprising ~10% of total $^{21}Ne_{excess}$.

Subtraction of $^{21}Ne_{mantle}$ (where the majority of mantle Ne is released at 500°C for most of the cases) and $^{21}Ne_{nucleo}$ from total $^{21}Ne_{excess}$ yields $^{21}Ne_c$ (Table 6). Calculated $^{21}Ne_c$ values attenuate exponentially with depth, ranging from $68.7 \pm 8.8 \times 10^6$ atom g^{-1} in TP13 (30 cm), to $\leq 1.6 \times 10^6$ atom g^{-1} in samples from greater than 2 m depth (TP6, TP5, TP4, TP15). Given that the effective attenuation length for fast neutrons in rocks of this density (2.96 g cm^{-3}) is ~54 cm (assuming Λ = 160 g cm^{-2} (Kurz, 1986)), the amount of spallogenic $^{21}Ne_c$ produced below ~2.5 m (5 attenuation lengths) is expected to be negligible, at <1 % of the surface concentration. Calculated $^{21}Ne_c$ concentrations in samples TP6 (350 cm), TP5 (460 cm) and TP4 (560 cm) are indistinguishable from zero considering the uncertainties, and are completely overwhelmed by coexisting $^{21}Ne_{nucleo}$ (Table 6). The deepest sample, TP15 (1100 cm), yields an apparently non-zero $^{21}Ne_c$ concentration of $1.56 \pm 0.65 \times 10^6$ atom g^{-1}, similar to the corresponding $^{21}Ne_{nucleo}$ value ($3.9 \pm 0.4 \times 10^6$ atom g^{-1}).

Calculated $^{21}Ne_c$ concentrations were used to determine an apparent Cenozoic erosion rate assuming a simple exposure history and steady-state erosion (section 5.5) for comparison with the $^{36}Cl_c$-determined erosion rate (see section 4.5).

5.4 Constraining the muogenic neon production rate in olivine

Previous investigations into muogenic neon production, as reviewed by Balco and Shuster (2009), have exclusively involved quartz, considering muon-capture reactions on Si only. By evaluating the neon content in quartz from slowly eroding Antarctic bedrock surfaces where secular equilibrium of cosmogenic nuclides (^{26}Al, ^{10}Be and ^{21}Ne) is considered to apply, Balco and Shuster (2009) report a total muogenic SLHL

production rate of 0.66 ± 0.10 (1σ) for ^{21}Ne in quartz. Fernandez-Mosquera et al. (2010) consider theoretical ^{21}Ne and ^{22}Ne production channels involving fast-muon induced reactions and slow-muon capture reactions on ^{28}Si, proposing that muogenic ^{21}Ne in quartz is dominantly produced by fast-muon induced reactions (e.g. ^{28}Si(μ, α2pn)^{21}Ne). Using attenuation lengths of Bruacher et al. (2003), they predict a SLHL fast muon production rate of ^{21}Ne of 0.39 ± 0.15 atom g^{-1} a^{-1} (1σ) in quartz, with fast muon production exceeding spallogenic ^{21}Ne production at *ca.* 3 m depth in quartz. A SLHL slow muon induced production rate of 0.12 ± 0.03 atom g^{-1} a^{-1} was proposed by Fernandez-Mosquera et al. (2010). They note that the SLHL production rates are within uncertainty of the total muogenic ^{21}Ne$_c$ production rate proposed by Balco and Shuster (2009).

In olivine, muogenic ^{21}Ne is predicted to derive from reactions on both Si and Mg, but we cannot separate these production rates in this study. Using the production rates of Fernandez-Mosquera et al. (2010), and the Si-content of olivine (17.9 wt. % Si, Table 2), minimum total SLHL production rates for fast-muon and slow-muon induced ^{21}Ne$_c$ components in olivine are calculated at 0.15 ± 0.06 atom g^{-1} a^{-1} (1σ) and 0.05 ± 0.01 (1σ) atom g^{-1} a^{-1}, respectively. The stated uncertainty in these values reflects only the error reported by Fernandez-Mosquera et al. (2010).

In the absence of constraints on the relative importance of fast-muon vs slow-muon capture reactions producing ^{21}Ne from isotopes of Mg, we determine an upper estimate for total muogenic ^{21}Ne production, assuming that it is mainly derived from fast-muon interactions. We input calculated ^{21}Ne$_c$ concentrations for the studied profile (Table 6) into the steady state erosion equation (Lal, 1991), optimising for both erosion rate and fast-muon production rate, using the approximations of Granger and Smith (2000) to describe muon attenuation with depth. Constants used in the calculation were: a fast neutron attenuation length of 160 g cm^{-2} (Kurz 1986), a fast muon attenuation length of 4360 g cm^{-2} (Granger and Smith, 2000), a density of 2.96 g cm^{-3}, and a site-specific spallogenic ^{21}Ne$_c$ production rate of 66 atom g^{-1} a^{-1} (section 4.2).

On the basis stated above, we calculate a fast-muon ^{21}Ne$_c$ production rate of 0.04 ± 0.07 atom g^{-1} a^{-1}, translating to a SLHL value of 0.02 ± 0.04 atom g^{-1} a^{-1} (1σ) using the fast muon scaling model of Stone (2000), and an apparent erosion rate at the site of 0.29 ± 0.02 m Ma^{-1} (based on the Ne systematics in the present study).

Uncertainties are standard error of the mean and exclude systematic uncertainties. Including slow muon production did not produce a realistic fit and is predicted to be insignificant. The modelled production rate of 0.02 ± 0.04 atom g^{-1} a^{-1} is within 2σ uncertainty of the theoretical SLHL fast-muon production rate predicted in olivine based on fast-muon reactions on ^{28}Si alone (0.15 ± 0.06 atom g^{-1} a^{-1}), and to the calculated $^{21}Ne_{nucleo}$ production rate (0.05–0.09 (± 10%) atom g^{-1} a^{-1}) in these samples. It suggests that ~0.1% of total cosmogenic ^{21}Ne in surface olivine at SLHL is produced from muon interactions.

5.5 Exposure history of the Thompson's Pit site

There is disagreement beyond estimated uncertainties for the apparent erosion rates calculated using the $^{21}Ne_c$ and ^{36}Cl results. An apparent erosion rate of 4.7 m Ma^{-1} was calculated from the $^{36}Cl_c$ depth concentration profile (cf. sections 4.5 and 5.4; Fig. 5), assuming steady state erosion (i.e. >3 m was eroded). This is consistent with previous estimates of ≤5 m Ma^{-1} for Cenozoic erosion in the south-eastern Highlands (Heimsath et al., 2001). The effective time period for this erosion rate is the last 500 ka. In contrast, the $^{21}Ne_c$ data, as discussed above, apparently reflect a very low long-term erosion rate of ~0.2 m Ma^{-1}, equivalent to an effective minimum exposure age (Lal, 1991) of 1.7 Ma. Such low erosion rates are unusual outside of desert environments and very hard rock types, indicating previous exposure and a complex exposure history for the site. One such scenario would be exposure of the basalt when it was erupted and all ^{36}Cl produced at this time has since eroded away. Under this scenario, the muon contribution we estimate would be a maximum However, even under this scenario, the fast muon contribution would be only 1.2 ± 1.8 atom g^{-1} a^{-1}, (1σ), scaling to 0.9 ± 1.3 atom g^{-1} a^{-1} (1σ) SLHL, <2.5% of spallogenic production. As noted by Gosse and Phillips (2001), low cosmogenic isotopic ratios involving a stable denominator (e.g. $^{36}Cl_c/^{21}Ne_c$), as observed in the present study, could be explained either by burial or episodic rapid erosion and therefore any modelling is highly speculative unless independent constraints on the burial history are available. As exposure history modelling at the Thompson's Pit site is under-constrained, the simplest explanation for apparent decoupling of the $^{36}Cl_c$ and $^{21}Ne_c$ concentration profiles is a long initial exposure period, followed by burial, and recent re-exposure. Importantly, it is stressed that the uncertainties surrounding the cosmogenic Ne

exposure history have no bearing on estimation of the muogenic production rate given the apparently long attenuation length of fast muons (4630 g cm^{-2} ; Granger and Smith (2000)).

6. Conclusions

Olivine extracted from a 12 m thick vertical profile was examined to determine whether muogenic ^{21}Ne was detectable. It was found that in olivine derived from >2 m depth, the ^{21}Ne remaining after correction of the trapped (magmatic) component is almost entirely accounted for by nucleogenic ^{21}Ne. The very small amounts of surplus ^{21}Ne detected in three deep (>2 m) samples suggest a muogenic $^{21}Ne_c$ SLHL production rate of 0.02 ± 0.04 to 0.9 ± 1.3 atom g^{-1} a^{-1} (1σ) in olivine, or <2.5% of spallogenic production. This validates the implicit assumption in previous studies that accumulation of muogenic $^{21}Ne_c$ in this mineral is minimal/negligible, even over timescales of several million years. This is an important finding given the large systematic uncertainties associated with cosmogenic nuclide exposure studies.

Acknowledgements

The authors thank: J Chappell for initial advice on the field site and assistance in the field; I MacDougall for providing petrographic descriptions; P Carr for XRF analysis (University of Wollongong); J Hughes and T Fujioka for assistance with mineral separation of olivine at the Australian National University; K Leslie and S Turner for assistance preparing samples in the Exeter Cosmogenic Nuclide Laboratory; A. Greig for undertaking trace element ICP-MS analyses (University of Melbourne) and J Hergt for discussions regarding these data. This work was supported by ARC Discovery grants DP0773815, DP0986235 and DP130100517. Constructive comments made by three anonymous reviewers were helpful in improving the quality of the manuscript.

References

Amidon, W.H., Rood, D.H. and Farley, K.A. (2009). Cosmogenic ^{3}He and ^{21}Ne production rates calibrated against ^{10}Be in minerals from the Coso volcanic field. *Earth Planet. Sci. Lett.* **280**, 194-204.

Andrews, J.N. (1985). The isotopic composition of radiogenic helium and its use to study groundwater movement in confined aquifers. *Chem. Geol.* **49**, 339-351.

Andrews, J.N., Kay, R.L.F. (1982). Natural production of tritium in permeable rocks. *Nature* **298**, 361-363.

Balco, G. and Shuster, D.L. (2009). Production rate of cosmogenic ^{21}Ne in quartz estimated from ^{10}Be, ^{26}Al, and ^{21}Ne concentrations in slowly eroding Antarctic bedrock surfaces. *Earth Planet. Sci. Lett.* **281**, 48-58.

Ballentine, C.J., Burnard, P.G., 2002. Production, Release and Transport of Noble Gases in the Continental Crust. *Rev. Mineral. Geochem.* **47**, 481–538.

Barrows, T.T., Stone, J.O. and Fifield, L.K. (2002). The timing of the Last Glacial Maximum in Australia. *Quat. Sci. Rev.* **21**, 159-173.

Barrows, T.T., Stone, J.O., Fifield, L.K. and Cresswell, R.G. (2001). Late Pleistocene glaciation of the Kosciuszko Massif, Snowy Mountains, Australia. *Quat. Res.* **55**, 179-189.

Benkert, J.-P., H. Baur, P. Signer, and IL Wider, 1993, He, Ne, and Ar from the solar wind and solar energetic particles in lunar ilmenites and pyroxenes. J. Geophys. Res. 98, 13147-13162.

Blard, P.-H. and Farley, K.A. (2008). The influence of radiogenic ^{4}He on cosmogenic ^{3}He determinations in volcanic olivine and pyroxene. *Earth Planet. Sci. Lett.* **276**, 20-29.

Blard, P.-H., Pik, R., Lavé, J., Bourlès, D., Burnard, P.G., Yokochi, R., Marty, B. and Tursdell, F. (2006). Cosmogenic ^{3}He production rates revisited from evidences of grain size dependent release of matrix-sited helium. *Earth Planet. Sci. Lett.* **247**, 222-234.

Braucher, R., Bourlès, D., Merchel, S., Romani, J.V., Fernandez-Mosquera, D., Marti, K., Léanni, L., Chauvet, F., Arnold, M., Aumaître, G. and Keddadouche, K. (2013). Determination of muon attenuation lengths in depth profiles from in situ produced cosmogenic nuclides. *Nucl. Instrum. Methods Phys. Res. B* **294**, 484-490.

Brown, E.T., Bourlès, D.L., Colin, F., Raisbeck, G.M., Yiou, F. and Desgarceaux, S. (1995). Evidence for muon-induced in situ production of ^{10}Be in near-surface rocks from the Congo. *Geophys. Res. Lett.* **22**, 703-706.

Dunai, T.J. (2000). Scaling factors for production rates of in situ produced cosmogenic nuclides: a critical reevaluation. *Earth Planet. Sci. Lett.* **176**, 157-169.

Dunai, T. J. (2010). *Cosmogenic Nuclides: Principles, Concepts and Applications in the Earth Surface Sciences*, 198 pp., Cambridge University Press.

Eberhardt, P., Eugster, O. and Marti, K. (1965). A redetermination of the isotopic composition of atmospheric neon. *Z. Naturforsch., A: Phys. Sci.* **20**, 623-624.

Eggins, S., Woodhead, J.D., Kinsley, L., Mortimer, G., Sylvester, P., McCulloch, M., Hergt, J.M. and Handler, M.R. (1997). A simple method for the precise determination of ≥ 40 trace elements in geological samples by ICPMS using enriched isotope internal standardisation. *Chem. Geol.* **134**, 311-326.

Espanon, V. R., M. Honda, and A. R. Chivas (2014), Cosmogenic ^{3}He and ^{21}Ne surface exposure dating of young basalts from Southern Mendoza, Argentina, *Quat. Geochronol.* **19**. 76-86.

Evans, J.M., 2001. Calibration of the production rates of cosmogenic ^{36}Cl from potassium. PhD thesis, The Australian National University, Canberra.

Fabryka-Martin, J.T., 1988. Production of radionuclides in the Earth and their hydrogeologic significance, with emphasis on chlorine-36 and iodine-129. PhD thesis, The University of Arizona. http://hdl.handle.net/10150/191140 311-326

Fernandez-Mosquera, D., Hahn, D. and Marti, K. (2010). Calculated rates of cosmic ray muon-produced Ne in subsurface quartz. *Geophys. Res. Lett.* **37**, LI5403.

Gillen, D., Honda, M., Chivas, A.R., Yatsevich, I., Patterson, D.B. and Carr, P.F. (2010). Cosmogenic ^{21}Ne exposure dating of young basaltic lava flows from the Newer Volcanic Province, southwestern Victoria, Australia. *Quat. Geochronol.* **5**, 1-9.

Goehring, B.M., Kurz, M.D., Balco, G., Schaefer, J.M., Licciardi, J. and Lifton, N. (2010). A reevaluation of in situ cosmogenic ^{3}He production rates. *Quat. Geochronol.* **5**, 410-418.

Gosse, J. and Phillips, F.M. (2001). Terrestrial in situ cosmogenic nuclides: theory and application. *Quat. Sci. Rev.* **20**, 1475-1560.

Graham, D.W. (2002). Noble gas isotope geochemistry of mid-ocean ridge and ocean island basalts; characterization of mantle source reservoirs. *Rev. Mineral. Geochem.* **47**, 247-318.

662 Granger, D.E., Smith, A.L., 2000. Dating buried sediments using radioactive decay and muogenic
663 production of ^{26}Al and ^{10}Be. Nuclear instruments and methods in physics, , Section B, Beam
664 Interactions with Materials and Atoms 172, 822–826.
665 Grimberg, A., Baur, H., Bochsler, P., Bühler, F., Burnett, D.S., Hays, C.C., Heber, V.S., Jurewicz, A.J.G.,
666 Wieler, R., 2006. Solar wind neon from Genesis: implications for the lunar noble gas record.
667 Science 314, 1133–1135.
668 Heimsath, A.M., Chappell, J., Dietrich, W.E., Nishiizumi, K. and Finkel, R.C. (2001). Late Quaternary
669 erosion in southeastern Australia; a field example using cosmogenic nuclides, *Quat. Int.* **83-85**,
670 169-185.
671 Heisinger, B., Lal, D., Jull, A.J.T., Kubik, P., Ivy-Ochs, S., Neumaier, S., Knie, K., Lazarev, V., Nolte, E.,
672 (2002a). Production of selected cosmogenic radionuclides by muons; 1, Fast muons. *Earth*
673 *Planet. Sci. Lett.* **200**, 345-355.
674 Heisinger, B., Lal, D., Jull, A.J.T., Kubik, P., Ivy-Ochs, S., Knie, K. and Nolte, E. (2002b). Production of
675 selected cosmogenic radionuclides by muons; 2, Capture of negative muons. *Earth Planet. Sci.*
676 *Lett.* **200**, 357-369.
677 Heisinger, B. and Nolte, E. (2000). Cosmogenic in situ production of radionuclides: Exposure ages
678 and erosion rates. *Nucl. Instrum. Methods Phys. Res. B* **172**, 790-795.
679 Honda, M., McDougall, I., 1998. Primordial helium and neon in the Earth—a speculation on early
680 degassing. *Geophys. Res. Lett.* **25**, 1951–1954.
681 Honda, M., McDougall, I., Patterson, D.B., Doulgeris, A. and Clague, D.A. (1993). Noble gases in
682 submarine pillow basalt glasses from Loihi and Kilauea, Hawaii: A solar component in the
683 Earth. *Geochim. Cosmochim. Acta* **57**, 859-874.
684 Kamber, B.S., Greig, A., Schönberg, R. and Collerson, K.D. (2003). A refined solution to Earth's
685 hidden niobium: implications for evolution of continental crust and mode of core formation.
686 *Precambrian Res.* **126**, 289-308.
687 Kesson, S. E. (1973), The primary geochemistry of the Monaro alkaline volcanics, southeastern
688 Australia- evidence for upper mantle heterogeneity, *Contrib. Mineral. Petrol.*, **42**, 93-108.
689 Kohn, B.P., Gleadow, A.J.W., Brown, R.W., Gallagher, K., O'Sullivan, P.B. and Foster, D.A. (2002).
690 Shaping the Australian crust over the last 300 million years: insights from fission track
691 thermotectonic imaging and denudation studies of key terranes. *Aust. J. Earth Sci.* **49**, 697-
692 717.
693 Kurz, M.D. (1986). In situ production of terrestrial cosmogenic helium and some applications to
694 geochronology. *Geochim. Cosmochim. Acta* **50**, 2855-2862.
695 Lal, D. (1987). Cosmogenic nuclides produced in situ in terrestrial solids. *Nucl. Instrum. Methods*
696 *Phys. Res. B* **29**, 238-245.
697 Lal, D. (1988). In situ-produced cosmogenic isotopes in terrestrial rocks. *Annu. Rev. Earth Planet.*
698 *Sci.* **16**, 355–388.
699 Lal, D. (1991). Cosmic ray labeling of erosion surfaces: *in situ* nuclide production rates and
700 erosion models. *Earth Planet Sci. Lett.* **104**, 424-439.
701 Lee, J.-Y., Marti, K., Severinghaus, J., Kawamura, K., Yoo, S.-S., Lee, J., Kim, J., 2006. A
702 redetermination of the isotopic abundances of atmospheric Ar *Geochim. Cosmochim. Acta* **70**,
703 4507–4512.
704 Leya, I., Busemann, H., Baur, H., Wieler, R., Gloris, M., Neumann, S., Michel, R., Sudbrock, F. and
705 Herpers, U. (1998). Cross sections for the proton-induced production of He and Ne isotopes
706 from magnesium, aluminium, and silicon. *Nucl. Instrum. Methods Phys. Res. B* **145**, 449-458.
707 Liu, B., Phillips, F.M., Fabryka-Martin, J.T., Fowler, M.M., Stone, W.D., 1994. Cosmogenic ^{36}Cl
708 accumulation in unstable landforms 1. Effects of the thermal neutron distribution. *Water*
709 *Resources Research* **30**, 3115-3125.
710 Ludwig, K., (2012). User's Manual for Isoplot 3.75. A Geochronological Toolkit for Microsoft Excel.
711 *Spec. Publ. No. 5, Berkeley Geochronology Center*, Berkeley, California.
712 Marrocchi, Y., Burnard, P.G., Hamilton, D., Colin, A., Pujol, M., Zimmermann, L. and Marty, B.
713 (2009). Neon isotopic measurements using high-resolution, multicollector noble gas mass
714 spectrometer: HELIX-MC. *Geochem. Geophys. Geosyst* **10**, Q04015.
715 Masarik, J. (2002). Numerical simulation of in-situ production of cosmogenic nuclides. *Geochim.*
716 *Cosmochim. Acta* **66**, A491.
717 Masarik, J. and Reedy, R.C. (1995). Terrestrial cosmogenic-nuclide production systematics
718 calculated from numerical simulations. *Earth Planet. Sci. Lett.* **136**, 381-395.
719 Matchan, E. and Phillips, D., (2011). New ^{40}Ar/^{39}Ar ages for selected young (<1 Ma) basalt flows of
720 the Newer Volcanic Province, southeastern Australia. *Quat. Geochronol.* **6**, 356-368.
721 Matsuda, J. (2002). The ^{3}He/^{4}He ratio of the new internal He Standard of Japan (HESJ). *Geochem.*
722 *J.* **36**, 191-195.

McDougall, I. and Harrison, T.M. (1999.) Geochronology and Thermochronology by the $^{40}Ar/^{39}Ar$ Method, 2nd ed.: Oxford University Press/USA, 269 p.
Niedermann, S., Schaefer, J.M., Wieler, R., Naumann, R., 2007. The production rate of cosmogenic 38Ar from calcium in terrestrial pyroxene. Earth and Planetary Science Letters 257, 596–608.
Norvick, M.S. (2011). Paleogene basalts prove early uplift of Victoria's Eastern Uplands. *Aust. J. Earth Sci.* **58**, 93-94.
O'Reilly, S. Y., and M. Zhang (1995), Geochemical characteristics of lava-field basalts from eastern Australia and inferred sources: connections with the subcontinental lithospheric mantle? *Contrib. Mineral. Petrol.* **121**, 148-170.
Phillips, D., Matchan, E.L., Honda, M., Kuiper, K.F., 2017. Astronomical calibration of $^{40}Ar/^{39}Ar$ reference minerals using high-precision, multi-collector (ARGUSVI) mass spectrometry. *Geochim. Cosmochim. Acta.* **196**, 351–369.
Poreda, R.J. and Cerling, T.E. (1992). Cosmogenic neon in Recent lavas from the Western United States. Geophys. Res. Lett. **19**, 1863-1866.
Protin, M., Blard, P.-H., Marroccchi, Y. and Mathon, F. (2016). Irreversible adsorption of atmospheric helium on olivine: a lobster pot analogy. *Geochim. Cosmochim. Acta*. **179**, 76-88.
Roach, I.C., McQueen, K.G., Brown, M.C. (1994). Physical and petrological characteristics of basaltic eruption sites in the Monaro Volcanic Province, southeastern New South Wales, Australia. *AGSO J. Aust. Geol. Geophys.* **15**, 381-394.
Sarda, P. Staudacher, T., Allegre, C.J. (1988) Neon isotopes in submarine basalts. *Earth Planet Sci Lett.* **91**, 73-88.
Schaefer, J., Ivy-Ochs, S., Wieler, R., Leya, I., Baur, H., Denton, G., Schluechter, C., 1999. Cosmogenic noble gas studies in the oldest landscape on earth: surface exposure ages of the Dry Valleys, Antarctica. *Earth Planet Sci Lett.* 179, 215–226.
Schaefer, J., Baur, H., Denton, G., Ivy-Ochs, S., Marchant, D., Schluechter, C., Wieler, R., 2000. The oldest ice on Earth in Beacon Valley, Antarctica: new evidence from surface exposure dating. Earth and Planetary Science Letters 179, 91–99.
Schimmelpfennig, I., Williams, A., Pik, R., Burnard, P., Niedermann, S., Finkel, R., Schneider, B. and Benedetti, L. (2011). Inter-comparison of cosmogenic in-situ ^{3}He, ^{21}Ne and ^{36}Cl at low latitude along an altitude transect on the SE slope of Kilimanjaro volcano (3°S, Tanzania). *Quat. Geochronol.* **6**, 425-436.
Singer, B.S., Wijbrans, J.R., Nelson, S.T., Pringle, M.S., Feeley, T.C. and Dungan, M.A. (1998). Inherited argon in a Pleistocene andesite lava: $^{40}Ar/^{39}Ar$ incremental-heating and laser-fusion analyses of plagioclase. *Geology* **26**, 427-430.
Steiger, R.H. and Jäger, E. (1977). Subcommission on geochronology: Convention on the use of decay constants in geo- and cosmochronology. *Earth Planet. Sci. Lett.* **36**, 359-362.
Stone, J.O. (2000). Air pressure and cosmogenic isotope production. *J. Geophys. Res.* **105**, 23,753-23,759.
Stone, J.O., Allan, G.L., Fifield, L.K., Cresswell, R.G., 1996a. Cosmogenic chlorine-36 from calcium spallation. *Geochim. Cosmochim. Acta* 60, 679-692.
Stone, J.O., Evans, J.M., Fifield, L.K., Cresswell, R.G., Allan, G.L., 1996b. Cosmogenic chlorine-36 production rates from potassium and calcium. *Radiocarbon* **38**, 170-171.
Stone, J.O.H., Evans, J.M., Fifield, L.K., Allan, G.L. and Cresswell, R.G. (1998). Cosmogenic chlorine-36 production in calcite by muons. *Geochim. Cosmochim. Acta* **62**, 433-454.
Taylor, G., Truswell, E.M., McQueen, K.G. and Brown, M.C. (1990). Early Tertiary palaeogeography, landform evolution and palaeoclimates of the Southern Monaro, N.S.W., *Australia. Palaeogeogr., Palaeoclimatol., Palaeoecol.* **78**, 109-134.
Tolstikhin, I.N., Kamensky, I., Tarakanov, S., Kramers, J., Pekala, M., Skiba, V., Gannibal, M. and Novikov, D. (2010). Noble gas isotope sites and mobility in mafic rocks and olivine. *Geochim. Cosmochim. Acta* **74**, 1436-1447.
Trull, T.W., Kurz, M.D., Jenkins, W.J. (1991). Diffusion of cosmogenic ^{3}He in olivine and quartz: implications for surface exposure dating. *Earth Planet. Sci. Lett.* **103**, 241-256.
Tucker, J.M., Mukhopadhyay, S., 2014. Evidence for multiple magma ocean outgassing and atmospheric loss episodes from mantle noble gases. *Earth Planet. Sci. Lett.* **393**, 254–265.
Vasconcelos, P.M., Knesel, K.M., Cohen, B.E., Heim, J.A., 2008. Geochronology of the Australian Cenozoic: a history of tectonic and igneous activity, weathering, erosion, and sedimentation. Australian Journal of Earth Sciences 55, 865-914.
Wellman, P. and McDougall, I. (1974a). Cainozoic igneous activity in eastern Australia. *Tectonophysics.* **23**, 49-65.
Wellman, P. and McDougall, I. (1974b). Potassium-argon ages on the Cenozoic volcanic rocks of New South Wales. *Aust. J. Earth Sci.* **21**, 247-272.

784 Wetherill, G.W. (1954). Variations in the isotopic abundance of neon and argon extracted from
785 radioactive materials. *Phys. Rev.* **96**, 679-683.
786 Yatsevich, I. and Honda, M. (1997). Production of nucleogenic neon in the Earth from natural
787 radioactive decay. *J. Geophys. Res*. **102**, 10,291-10,298.
788

Table 1. Summary of results from $^{40}Ar/^{39}Ar$ furnace step-heating analyses on whole-rock samples

	Age spectrum					Inverse Isochron analysis					Total gas age (ka) ± 2σ
Aliquot	Steps used	^{39}Ar (%)	MSWD	*p*	Age (ka) ± 2σ [a]	$^{40}Ar/^{36}Ar_i$ ± 2σ	MSWD	*p*	Age (ka) ± 2σ	n	
TP9 (1.6 m)											
TP9a	6–8	54	1.4	0.3	54.55±0.27	381±35	1.1	0.4	53.63±0.80	8	55.44±0.96
TP9b	5–8	67	2.2	0.1	55.35±0.35	446±100	0.6	0.6	54.65±0.86	4	55.96±0.78
TP5 (4.6 m)						*Mean inverse isochron age:*	3.2	0.1	*54.00±0.61*	2	
TP5a	5–8	63	1.1	0.4	55.17±0.34	502±150	0.7	0.6	52.6±2.5	6	55.78±0.91
TP5b	5–8	66	1.9	0.1	55.20±0.40	316±12	1.9	0.1	54.86±0.72	8	55.60±0.95
TP15 (11.1 m)						*Mean inverse isochron age:*	*3.8*	*0.1*	*54.55±0.66*	*2*	
TP15a	4–8	95	1.0	0.4	54.70±0.36	333±21	0.78	0.6	53.96±0.67	7	55.11±0.99
TP15b	1–8	100	1.3	0.2	55.59±0.44	331±50	0.18	1.0	54.5±1.3	7	55.5±1.5
						Mean inverse isochron age:	*0.66*	*0.4*	*53.96*±0.62	***2***	
						Mean inverse isochron age (TP9, TP5, TP15):	*1.1*	*0.3*	*54.15*±0.36	3	

[a]Ages have been calculated using the decay constants of Steiger and Jäger (1977), assuming an age of 99.125 ± 0.038 Ma for MD2 biotite (Phillips et al., 2017). Errors include uncertainty in the J-value.
[b]Mean inverse isochron ages for each sample are calculated by averaging the ($^{40}Ar/^{39}Ar$) ratios for each aliquant. Stated errors incorporate uncertainty in the J-value.

Table 2. Major element composition of TP olivine separates (ox. wt %)

Oxide	TP10 (ARC184)	TP12 (ARC186B)	TP13 (ARC187B)	TP15 (ARC188B)	Average
SiO_2	39.37	37.48	37.52	38.98	38.34
TiO_2	0.61	0.59	0.44	1.64	0.82
Al_2O_3	1.83	1.55	1.22	2.04	1.66
Fe_2O_3	24.78	24.16	28.20	25.12	25.57
MnO	0.33	0.31	0.36	0.34	0.34
MgO	27.66	27.15	30.00	24.97	27.45
CaO	4.92	4.74	1.84	5.98	4.37
Na_2O	0.16	0.18	0.09	0.21	0.16
K_2O	0.05	0.04	0.06	0.05	0.05
P_2O_5	0.05	0.06	0.07	0.09	0.07
SO_2	<0.01	<0.01	<0.01	<0.01	<0.01
Total	*99.76*	*96.27*[a]	*99.80*	*99.42*	*98.81*
Fo-content	68.9	69.0	67.8	66.3	68.0

[a] Low total oxide wt. % value determined for olivine sample TP12 does not significantly impact production rate estimates.

Table 3. Whole-rock chemical data and calculated ^{36}Cl components

Sample	Depth (cm)	[CaO] (wt%)[1]	[K_2O] (wt%)	[Fe_2O_3] (wt%)	[TiO_2] (wt%)	[Cl] (ppm)
TP16	5	9.06 ± 0.08	1.30 ± 0.039	9.18 ± 0.15	2.28 ± 0.06	5.95 ± 0.45
TP12	60	8.76 ± 0.08	1.24 ± 0.037	9.86 ± 0.16	2.17 ± 0.06	6.14 ± 0.45
TP11	110	9.46 ± 0.09	1.22 ± 0.037	8.58 ± 0.14	2.17 ± 0.06	5.47 ± 2.14
TP10	160	8.79 ± 0.08	1.24 ± 0.037	10.11 ± 0.17	2.15 ± 0.06	7.39 ± 0.48

Sample	Lab code	Depth (cm)	$[^{36}Cl]_c$ ($\times 10^5$ g^{-1})	$[^{36}Cl]_r$ ($\times 10^3$ g^{-1})
TP16	ANU-C190-22	5	9.104 ± 0.185	1.03 ± 0.09
TP12	ANU-C190-23	60	4.075 ± 0.091	1.01 ± 0.09
TP11	ANU-C264-23	110	2.251 ± 0.056	0.91 ± 0.40
TP10	ANU-C191-05	160	1.851 ± 0.106	1.18 ± 0.09

Λ = 160 $g.cm^{-2}$; Density = 2.96 $g.cm^{-3}$ as measured by water displacement. Data are normalised to the GEC standard ($^{36}Cl/Cl = 444 \times 10^{-15}$). Carrier $^{36}Cl/Cl = 1 \times 10^{-15}$. ^{36}Cl decay constant 2.3×10^{-6} a^{-1}. $[^{36}Cl]_c$ = cosmogenic component; $[^{36}Cl]_r$ = background nucleogenic component.

799 **Table 4.** Summary of helium and neon isotopic compositions for olivine aliquots (n=8)

Sample, mass	Temp (°C)	$^{4}He_{meas}$ (10^{12} atom g^{-1})	±1σ	$^{3}He_{meas}$ (10^{6} atom g^{-1})	±1σ	$^{3}He/^{4}He$ (10^{-9})	±1σ	^{20}Ne (10^{9} atom g^{-1})	±1σ	$^{21}Ne/^{20}Ne$	±1σ	$^{22}Ne/^{20}Ne$	±1σ
TP13	500	6.74	0.17	2.2	0.4	328	65	0.839	0.052	0.00315	0.00013	0.1017	0.0024
	1900	86.2	2.1	16.3	0.7	189	7	13.36	0.82	0.00839	0.00037	0.1082	0.0046
0.990g	Total	92.9	2.2	18.5	0.9	199	8	14.2	0.82	0.00808	0.00035	0.1078	0.0044
TP12	500	5.14	0.13	2.1	0.6	410	116	0.372	.060	0.00343	0.00020	0.1008	0.0035
	1900	77.7	2.0	11.7	0.9	151	11	10.40	0.60	0.00813	0.00044	0.1079	0.0057
0.856g	Total	82.8	2.0	13.8	1.1	167	13	10.78	0.60	0.00797	0.00043	0.1076	0.0055
TP11	500	9.52	0.24	4.0	0.5	418	55	0.227	0.029	0.00385	0.00035	0.1071	0.0029
	1900	70.5	1.8	15.2	0.8	216	10	0.764	0.030	0.03922	0.00122	0.1173	0.0035
0.923g	Total	80.0	1.8	19.2	1.0	240	11	0.991	0.041	0.03114	0.00126	0.1150	0.0028
TP10	500	5.30	0.13	0.6	0.4	113	84	0.295	0.035	0.00315	0.00026	0.1247	0.0034
	1900	72.6	1.8	6.5	0.4	90.1	5.2	1.225	0.062	0.00618	0.00029	0.1079	0.0047
1.020g	Total	77.9	1.8	7.1	0.6	91.7	7.5	1.52	0.072	0.00559	0.00025	0.1112	0.0039
TP6	500	12.7	0.3	1.4	0.6	109	44	0.292	0.043	0.00343	0.00036	0.0882	0.0042
	1900	52.4	1.3	4.7	0.8	90.3	15.4	1.141	0.051	0.00545	0.00022	0.1050	0.0039
0.868g	Total	65.1	1.3	6.1	1.0	94.0	15.0	1.433	0.066	0.00504	0.00019	0.1016	0.0033
TP5	500	15.1	0.4	1.9	0.4	126	23	0.4107	0.0323	0.00443	0.00026	0.0881	0.0039
	1900	97.7	2.4	4.5	0.5	45.8	4.9	1.629	0.056	0.00553	0.00017	0.1068	0.0029
0.858g	Total	113.0	2.5	6.4	0.6	56.5	5.3	2.040	0.060	0.00531	0.00014	0.1030	0.0025
TP4	500	10.6	0.3	0.3	0.7	26.6	62.7	0.5429	0.044	0.00324	0.00019	0.0945	0.0027
	1900	80.9	2.0	4.3	1.1	53.5	13.2	1.66	0.065	0.00499	0.00016	0.1053	0.0026
0.833g	Total	91.5	2.0	4.6	1.3	50.3	13.7	2.203	0.080	0.00456	0.00013	0.1026	0.0021
TP15	500	12.0	0.3	0.7	0.3	62.2	26.9	0.3921	0.05	0.00373	0.00033	0.0975	0.0036
	1900	83.8	2.1	2.3	0.5	26.9	6.1	0.879	0.042	0.00898	0.00038	0.1066	0.0044
0.884g	Total	95.7	2.1	3.0	0.6	31.3	6.3	1.271	0.066	0.00736	0.00032	0.1038	0.0032
Atmosphere[a]						1400				0.00296		0.102	
Cosmogenic Ne in olivine										1.3		1.2	

800 [a] Atmospheric neon composition (Eberhardt et al., 1965)
801 [b] Cosmogenic neon production ratio for olivine (Schaefer et al., 1999)
802

803 **Table 5.** Theoretical $^{4}He^{*}$, $^{21}Ne_{nucleo}$, $^{3}He_{nucleo}$ and $^{21}Ne_{excess}$ in olivine

Sample		U (ppm)	Th (ppm)	Li (ppm)	Predicted $^{3}He_{nucleo}$ (10^{6} atom/g)	Predicted $^{4}He^{*}$ (10^{12} atom/g)[a]	Measured total ^{4}He (10^{12} atom/g)	Predicted $^{21}Ne_{nucleo}$ (10^{6} atom/g)[b]	Measured total ^{21}Ne (10^{6} atom/g)	Predicted $^{21}Ne_{nucleo}$ in total measured ^{21}Ne (%)
TP13	ol	0.12	0.43	7.37	0.76	71	93	3.9	114.8	3.4
	gm	1.65	7.03	7.88						
TP12	ol	0.07	0.26	6.58	0.70	55	83	3.3	85.9	3.8
	gm	1.63	6.95	6.94						
TP6	ol	0.16	0.45	6.44	0.57	74	65	2.8	7.2	39
	gm	1.49	6.4	6.66						
TP5	ol	0.29	0.96	8.77	0.70	114	113	4.7	10.8	43
	gm	1.48	6.17	6.3						
TP4	ol	0.27	0.92	10.4	0.85	112	92	3.8	10.0	38
	gm	1.57	6.77	7.92						
TP15	ol	0.22	0.82	12.65	1.05	99	96	3.9	9.4	42
	gm	1.53	6.45	7.82						

804 Note: '-' denotes no available data
805 [a] Mean grain diameter of 500 μm was assumed for olivine phenocrysts in order to calculate net $^{4}He^{*}$ production, incorporating loss/implantation (Blard and Farley, 2008).
806 [b] Concentrations of $^{21}Ne_{nucleo}$ were inferred from calculated intra-phenocryst $^{4}He^{*}$ concentration values as described in the text.
807 [c] Production rate of $^{3}He_{nucleo}$ in olivine was calculated using the method of Andrews (1985). Neutron capture probabilities specific to individual sample compositions (namely Li, Na, Mg, Al, Si, Ca, U and Th) were
808 calculated using nuclear cross-section values reported by Andrews and Kay (1982).
809
810 T**able 6.** Excess ^{21}Ne components in olivine

Sample	Depth (cm)	$^{21}Ne_{excess}$	±1σ	$^{21}Ne_{mantle}$	±1σ	$^{21}Ne_{nucleo}$	±1σ[a]	$^{21}Ne_{c}$	±1σ	$^{21}Ne_{c}$ in $^{21}Ne_{excess}$ (%)
TP13	30	72.61	0.88	0.022	0.001.	3.9	0.4	68.7	8.8	95
TP12	60	53.39	0.69	0.036	0.006.	3.3	0.3	50.6	7.0	94
TP6	350	3.25	0.40	0.32	0.05	2.8	0.3	0.45	0.49	14
TP5	460	4.77	0.45	0.46	0.04	4.7	0.5	0.06	0.65	1
TP4	560	3.77	0.46	0.33	0.03.	3.8	0.4	-0.03	0.60	0
TP15	1110	5.47	0.52	0.14	0.02.	3.9	0.4	1.56	0.65	29

811 Note: concentrations expressed as 10^{6} atoms g^{-}
812 [a] Error for $^{21}Ne_{nucleo}$ is estimated at 10% (1σ).

FIGURE CAPTIONS

Fig. 1. Simplified geological map of the Nimmitabel-Bombala region in the Eastern Highlands of Australia. Location of Thompson's Pit (TP) indicated by star.

Fig. 2. Thompson's Pit. (a) Gradational weathering cap of soil transitioning to fresh basalt is >2 m in opposing quarry wall. (b) Profile sampled for the present study.

Fig. 3. Neon three-isotope plot showing results from step-heating experiments on 8 olivine aliquots from the Thompson's Pit basalt. A mixing line between cosmogenic neon (Schaefer et al., 1999) and atmospheric neon is shown. For comparison, the MORB correlation line (Sarda et al., 1988) and the mass-fractionation line for air (MFL) are also shown.

Fig. 4. Depth concentration profile for ^{21}Ne components and total measured ^{3}He concentrations ($^{3}He_{meas}$) in TP olivine samples. $^{21}Ne_c$ is defined as the residual ^{21}Ne concentration following subtraction of the magmatic neon component and *in situ* produced nucleogenic neon. Note that the $^{21}Ne_c$ concentrations for and TP6, TP5 and TP4 are $<1 \times 10^6$ atom g^{-1}; therefore, these values do not display on the partial logarithmic scale. Error bars are 1σ.

Fig 5. Comparison of depth concentration profiles for cosmogenic ^{21}Ne and ^{36}Cl in TP olivine and whole-rock, respectively. Errors are 1σ. Note that $^{21}Ne_c$ concentrations are plotted on a logarithmic scale and $^{36}Cl_c$.concentrations are plotted on a linear scale..

Figure 1

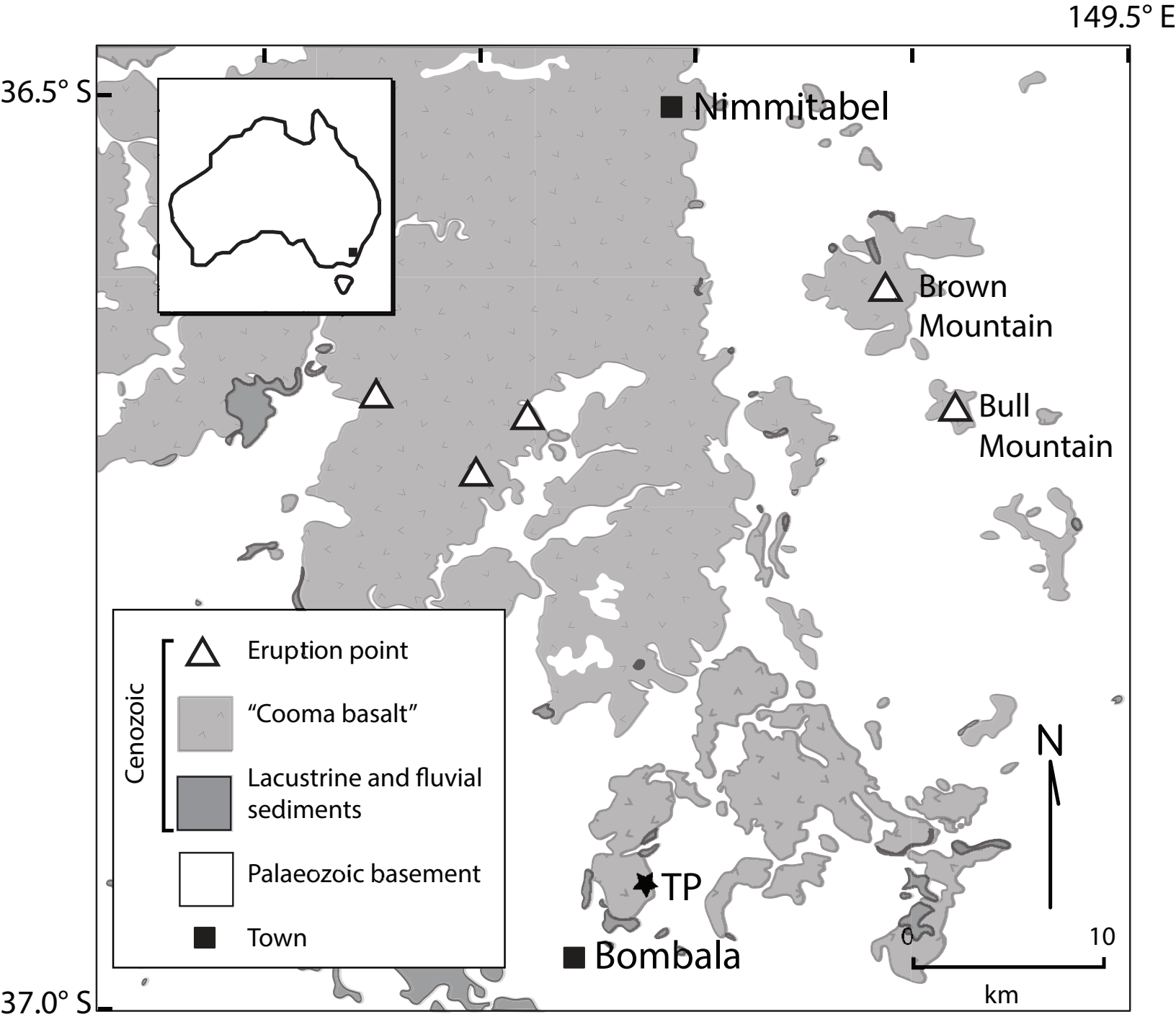
149.5° E
36.5° S
37.0° S
Nimmitabel
Brown Mountain
Bull Mountain
TP
Bombala
Cenozoic
Eruption point
"Cooma basalt"
Lacustrine and fluvial sediments
Palaeozoic basement
Town
N
0
10
km

Figure 2

Click here to download high resolution image

Figure 3

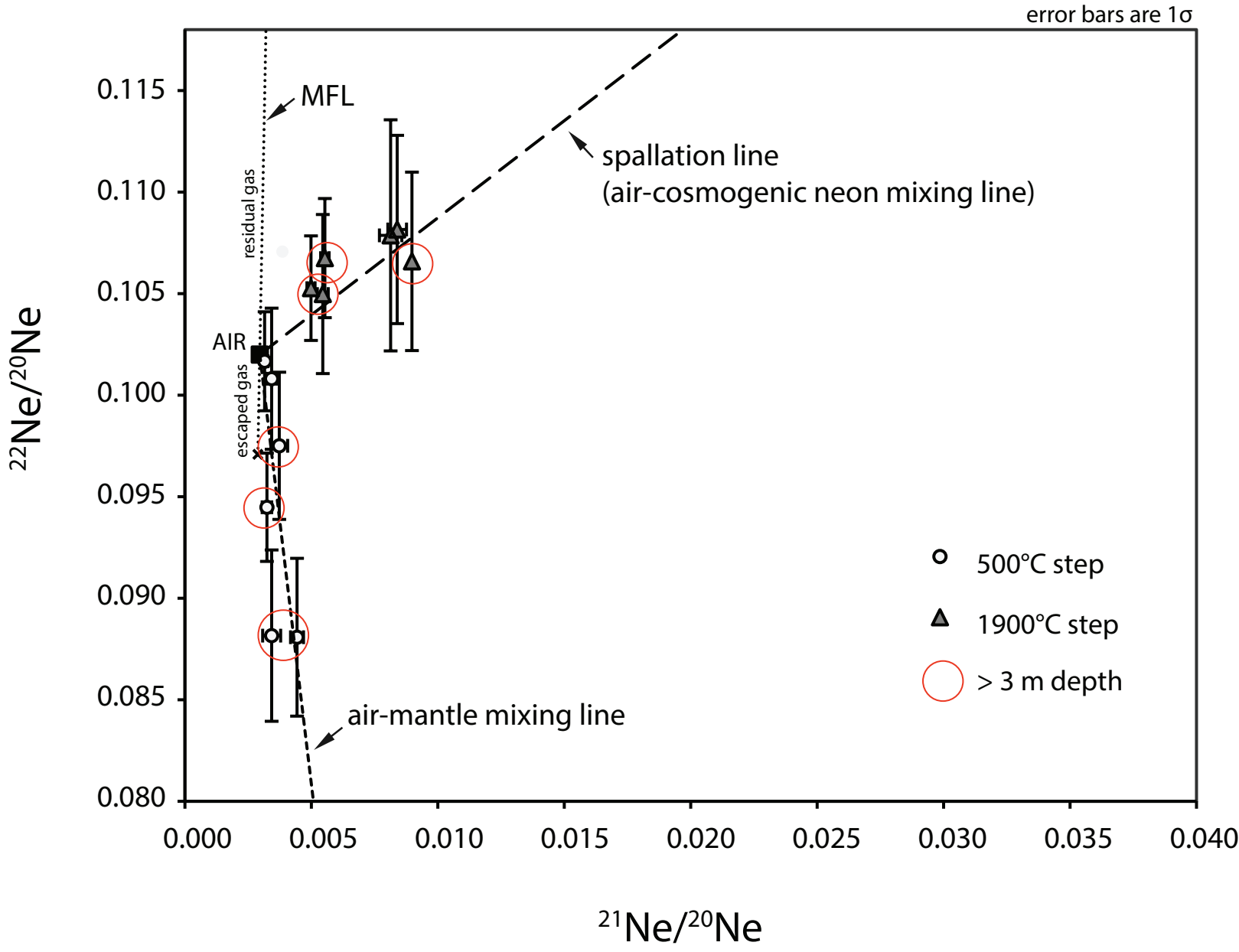
error bars are 1σ
MFL
spallation line
(air-cosmogenic neon mixing line)
residual gas
AIR
escaped gas
air-mantle mixing line
500°C step
1900°C step
> 3 m depth
0.115
0.110
0.105
0.100
0.095
0.090
0.085
0.080
0.000
0.005
0.010
0.015
0.020
0.025
0.030
0.035
0.040
22Ne/20Ne
21Ne/20Ne

Figure4_rev

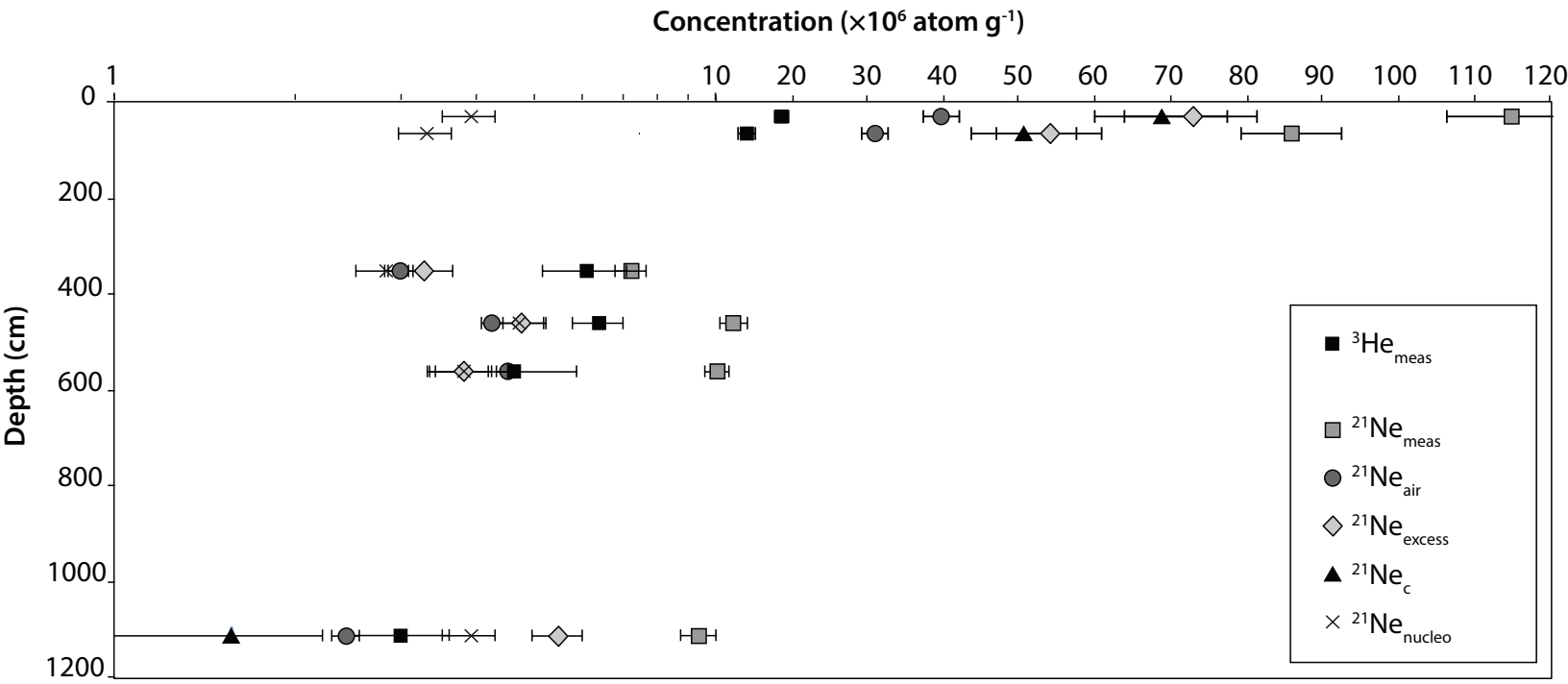
Concentration (×10⁶ atom g⁻¹)
1
10
20
30
40
50
60
70
80
90
100
110
120
0
200
400
600
800
1000
1200
Depth (cm)
³He meas
²¹Ne meas
²¹Ne air
²¹Ne excess
²¹Ne c
²¹Ne nucleo

Figure5_rev

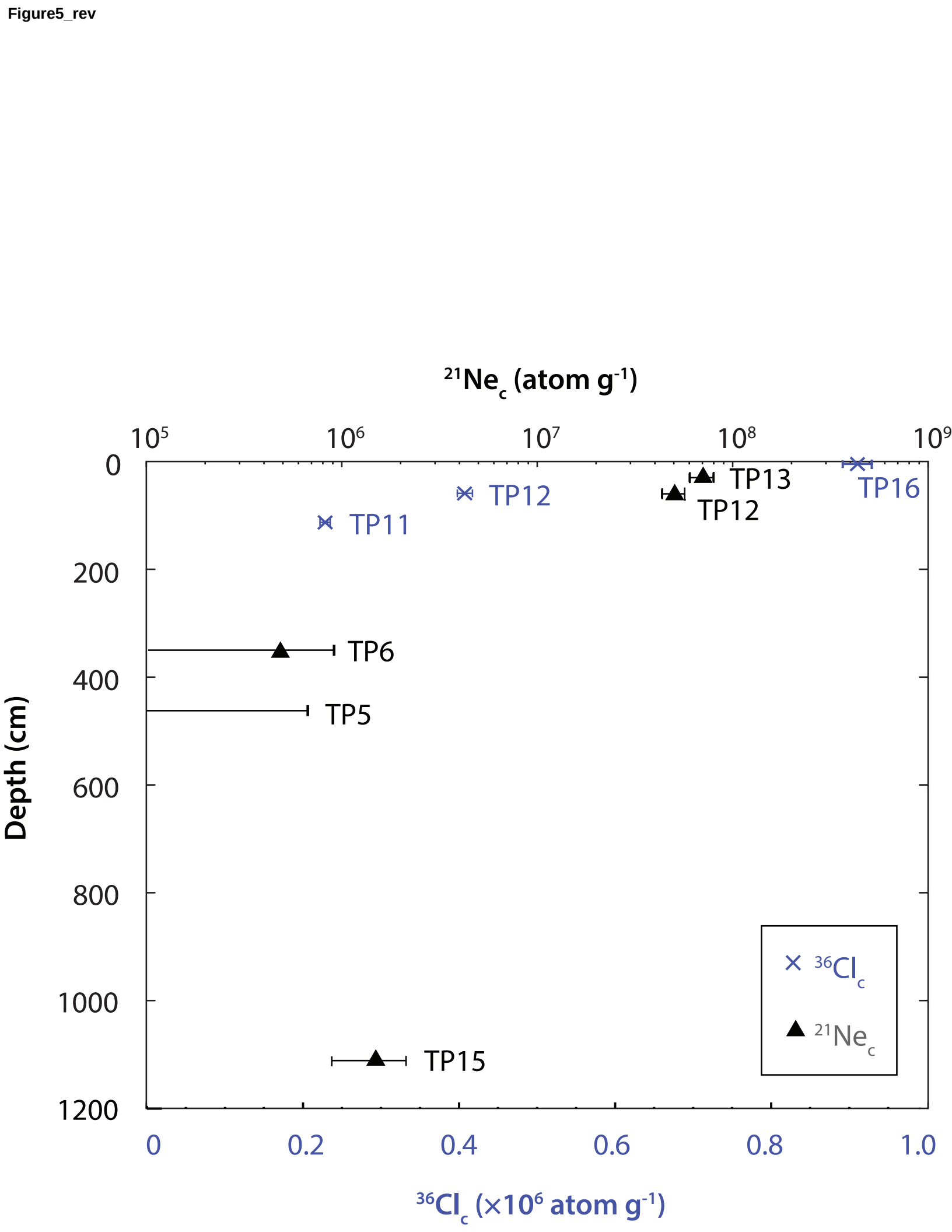
$^{21}Ne_c$ (atom g^{-1})
10^5
10^6
10^7
10^8
10^9
0
200
400
600
800
1000
1200
Depth (cm)
TP11
TP12
TP12
TP13
TP16
TP6
TP5
TP15
$^{36}Cl_c$
$^{21}Ne_c$
0
0.2
0.4
0.6
0.8
1.0
$^{36}Cl_c$ (×10^6 atom g^{-1})

Equations summary

$$^{3}He_c = {}^{3}He_T - \left[\left({}^{4}He_T - {}^{4}He^{*}\right) \times \left(\frac{^{3}He}{^{4}He}\right)_{mag}\right] - {}^{3}He_{nucleo} \quad (1)$$

$$^{21}Ne_{excess} = {}^{20}Ne_{meas} \times [(^{21}Ne/^{20}Ne)_{meas} - (^{21}Ne/^{20}Ne)_{air}] \quad (2)$$